International Journal of Fatigue 204 (2026) 109389

Contents lists available at ScienceDirect

International Journal of Fatigue

journal homepage: www.elsevier.com/locate/ijfatigue

Fatigue performance of a wheel steel under rotating bending and ultrasonic axial cycling: Role of elongated sulfides, effects of loading type and stress ratio

Hang Su [b,1], Lu Liu [a,c,1], Runjie Yang [d,1], Zhiying Chen [e], Shengnan Wang [c], Qing Peng [f], Xiangnan Pan [g,*]

[a] School of Aircraft, Xihang University, Xi'an 710000, China
[b] Department of Civil Engineering, University of California, Los Angeles, CA 90095, USA
[c] School of Aeronautics, Northwestern Polytechnical University, Xi'an 710072, China
[d] School of Electrical Engineering and Automation, Harbin Institute of Technology, Harbin 150001, China
[e] Key Laboratory of Pressure Systems and Safety (DOE), School of Mechanical and Power Engineering, East China University of Science and Technology, Shanghai 200237, China
[f] School of Power and Mechanical Engineering, Wuhan University, Wuhan 430072, China
[g] LNM, Institute of Mechanics, Chinese Academy of Sciences, Beijing 100190, China

ARTICLE INFO

Keywords:
Very-high-cycle fatigue
Crack initiation
Sulfide inclusion
Stress ratio
Rotating bending
Ultrasonic loading
Wheel steel

ABSTRACT

In this paper, a wheel steel, with a relatively low tensile strength and a distinct yield strength, is systematically investigated for high-cycle and very-high-cycle fatigue (failure life $N_f > 10^7$ cycles) under rotating bending (RB, 52.5 Hz) and ultrasonic axial cycling (UAC, ~ 20 kHz) with stress ratios $R = -1$ and 0.3. This work provides the first systematic evaluation of a medium-strength wheel steel commonly used in railway applications. All cracks initiated from the specimen surface and failures were limited to the HCF regime in RB tests while UAC tests revealed sulfide-induced failures, occurring both at the surface and in the interior, and extending into the VHCF regime. Microstructural analysis demonstrated nanograin formation and refinement near inclusions under $R = -1$, and partial cementite dissolution under $R = 0.3$, indicating stress-ratio-dependent initiation mechanisms. Furthermore, the fatigue limit followed a Gerber-type relation constrained by yield strength, and a probability-based failure map was established to quantify the occurrence of different failure modes. These findings extend the current understanding of VHCF beyond martensitic steels, clarify the role of elongated sulfides in wheel steels, and provide engineering insight into the fatigue reliability of railway wheels.

1. Introduction

It is well known that very-high-cycle fatigue [1–6] (VHCF, failure life $N_f > 10^7$ cycles) can occur in high-strength materials [7–11], in which specimen surface dominates low-cycle and high-cycle fatigue (HCF), whereas specimen subsurface or interior usually dominates VHCF. Among typical high-strength materials, age-hardenable nickel-based superalloys (e.g. IN718 [12]) or high-carbon steels (e.g. GCr15 [13]) can readily achieve an ultimate tensile strength (UTS) $\sigma_u > 1$ GPa through solution/aging or quenching/tempering, respectively, to form strengthened microstructure (e.g. tempered martensite), with no yield plateau observed.

In 1983 and 1984, Naito et al. [14,15] performed carburizing on a low-carbon steel (SCM 415: 0.16C by weight percent), followed by oil-quenching and low-temperature tempering at 180°C. The hardness of the carburized layer reaches approximately 750 HV. Through rotating bending (RB) fatigue tests, S-N data ranging from 10^4 to 10^8 cycles were obtained. The fitted Wöhler curve [16,17] is step-shaped with two knee points: one is at approximately 10^5 cycles, and the other is at about 5×10^6 cycles, with an approximately horizontal segment between them. They reported the specimens continued to fail over 10^7 cycles, i.e. VHCF for the first time in carbon steels. When the carburized layer is removed via electrolytic polishing, the fatigue strength improves significantly, and failures can occur under both HCF and VHCF conditions. For failed

* Corresponding author.
E-mail address: panxiangnan@lnm.imech.ac.cn (X. Pan).
[1] These authors contributed equally to this work.

https://doi.org/10.1016/j.ijfatigue.2025.109389
Received 12 August 2025; Received in revised form 14 October 2025; Accepted 9 November 2025
Available online 10 November 2025

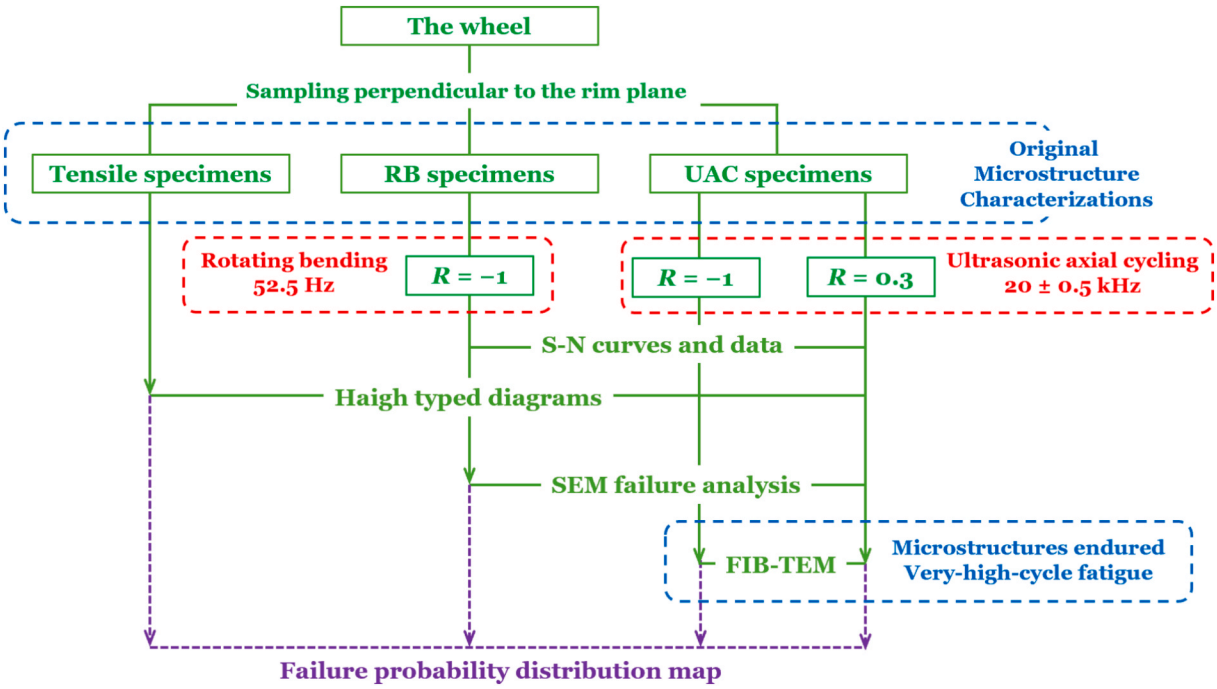

Fig. 1. Flowchart of fatigue testing and microstructural characterization for the wheel.

specimens of $N_f > 10^6$ cycles, the fracture surface frequently exhibits a "fish eye (FiE)" morphology originating from nonmetallic inclusions at specimen interior.

After over 40 years of research on VHCF [18–23], it has now been basically clarified that for high-strength steels with tempered martensites, of which $\sigma_u > 1.5$ GPa, whether under RB loading or other axial tension–compression types (all corresponding to a stress ratio $R = -1$), the distribution of their S-N data presents a similar stepwise or duplex shape. The first slope corresponds to low-cycle and HCF induced by surface crack initiation, while the second slope corresponds to high-cycle and VHCF induced by subsurface or internal FiE fracture.

Fatigue testing [24] is time-consuming and labor-intensive, especially for VHCF. Due to the advantage of loading frequency, ultrasonic axial cycling (UAC) had been widely adopted by VHCF researchers [21,25]. However, this will inevitably raise a question [13,26–30]: what impact does such a high loading frequency itself exert – specifically, ultrasonic frequencies around 20 kHz versus conventional ones on the order of below 100 Hz – on HCF and VHCF behavior?

In VHCF regime, crack initiation and early growth predominantly accounts for over 90 % of the total fatigue life [22,31,32]. For high-strength steels, the fracture surfaces of specimens failed by VHCF loading exhibit a characteristic region of crack initiation, which appears as an "optical dark area (ODA, [18])" under optical microscopy (OM) and a "fine granular area (FGA, [19])" under scanning electron microscopy (SEM). By using focused ion beam (FIB), transmission electron microscopy (TEM) and other advanced characterization techniques, many investigators [33–43] have identified the microstructure underneath the fracture surface of crack initiation region in various metallic materials endured VHCF loading. It has been consistently confirmed that under a negative stress ratio of $R = -1$, there exist phenomena of microstructure refinement and nanograin formation. Recently, Hong et al. [34] identified that in high-strength steels, this phenomenon correlates with the stress ratio and fatigue life: as the stress ratio increases or the fatigue life decreases, the fine granules gradually become indistinct and even vanish entirely, whereas microstructure refinement weakens and the original coarse grains remain intact.

Note that the term "high-strength" remains notably ambiguous. Even for high-strength steels [44–48], the critical tensile properties often fluctuate within a very wide range, such as the UTS σ_u, yield strength σ_y or 0.2 % proof stress $\sigma_{0.2}$ (engineering stress at a residual engineering strain of 0.2 %). Conventionally, high-strength steel is defined differently across various industries [49]: in the automotive sector, steel with a yield strength σ_y or $\sigma_{0.2}$ of 270–550 MPa is classified as "high-strength", while that with a yield strength exceeding 550 MPa is designated as ultra-high-strength steel; in construction and bridge engineering, high-strength steel is typically defined by $\sigma_u \geq 490$ MPa; and in the aerospace field, the threshold for high-strength steel may be elevated to a yield strength of ≥ 800 MPa. However, high-strength steels [13,19,20,27,31,33–35,49] – traditionally recognized as exhibiting VHCF characteristics – typically require the UTS values exceeding 1.5 GPa, and in some cases even reaching 1.7 GPa [13]. Their strengthened structure is all tempered martensite. This has resulted in an obvious strength gap between these two categories of so-called "high-strength steels", and the wheel steel studied in this paper falls exactly within this range.

Due to the complex service environment, railway or high-speed rail track steels [50–53] demand materials with adequate strength and toughness; therefore, bainite/martensite dual phases or a standalone bainitic structure are commonly employed. Bainitic steel has slightly lower strength than tempered martensite. To prioritize the protection of railway tracks, the interacting wheels are designed to have even lower strength, with the contact surface of their outermost tread maintaining a tensile limit of less than 1 GPa and a Vickers hardness in the range of 280–290 [52,54]. Thus, the carbon content (0.5 ~ 0.8 % by weight) of wheel steel places it between medium-carbon and high-carbon steels, and it is generally heat-treated to form a microstructure consisting of pearlite [54–57] or bainite [58,59].

To date, while there have been some studies on the VHCF of carbon steels [39,55,56] and alloy steels [36,37,60] with a UTS of around 1 GPa, the number of such studies remains far from sufficient. Specifically, structural steels with moderate strength, especially those with ferrite–pearlite microstructures, have received much less attention despite their widespread use in engineering applications. Railway wheel steels, in particular, experience complex cyclic loading and service lives exceeding 10^8–10^9 cycles, making VHCF behavior highly relevant to their safety and durability. However, existing VHCF studies on wheel

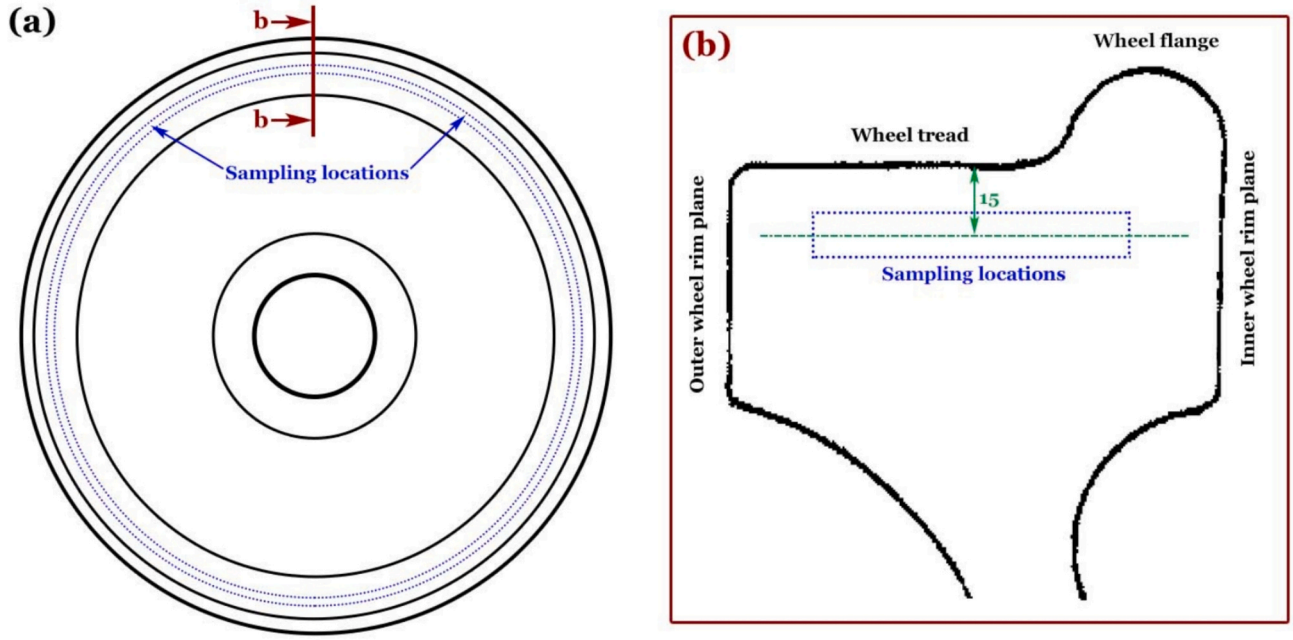

Fig. 2. Schematic presentation of the sampling locations from the wheel: (a) front view, (b) local enlarged view of the radial section at position b in (a).

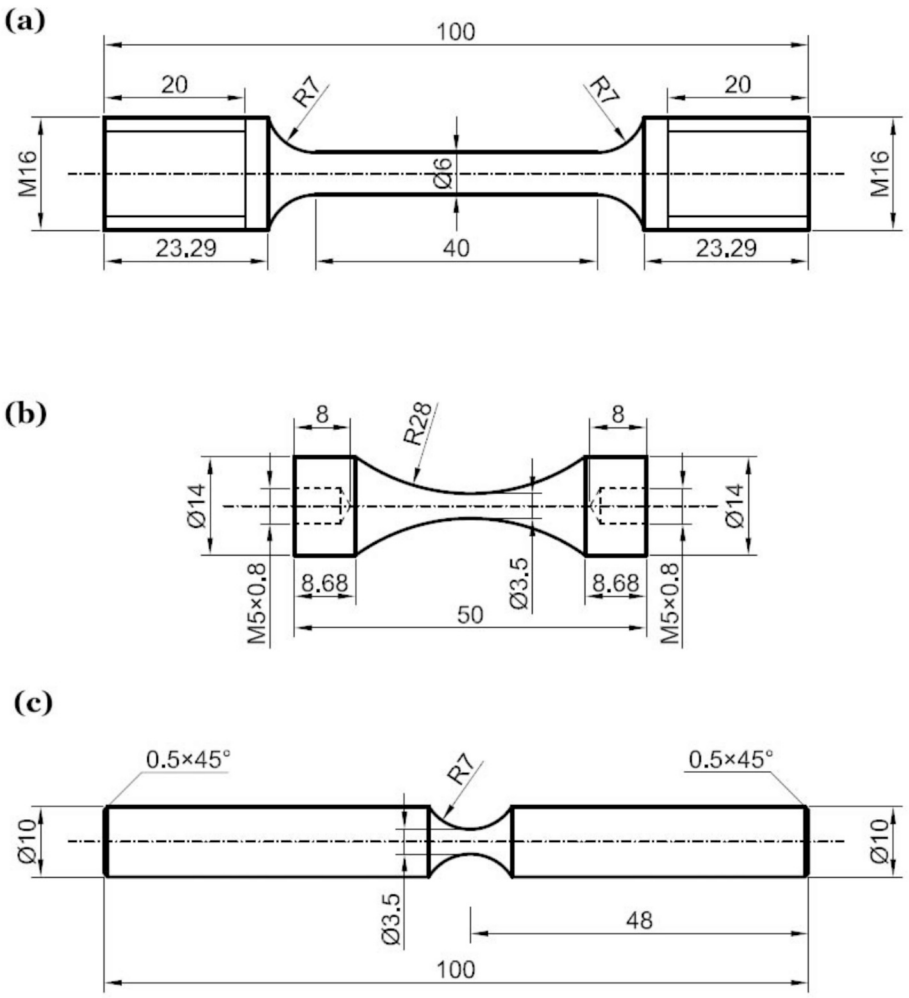

Fig. 3. Specimen geometries (dimension in mm) for quasi-static tension (a), ultrasonic cycling (b), and rotating bending (c).

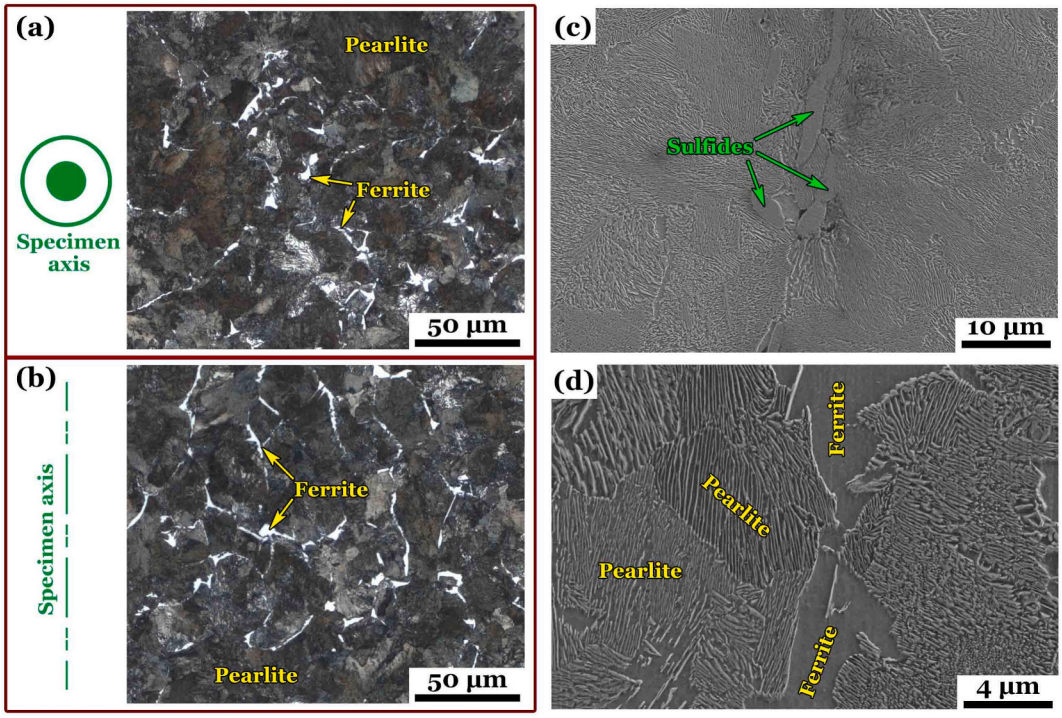

Fig. 4. Optical micrographs of latitudinal (a) and longitudinal (b) sections using optical microscopy and scanning electron microscopy at medium (c) and high (d) magnifications.

steels remain limited, and the mechanisms governing fatigue failure under different loading types and stress ratios are not yet clearly understood.

To address this gap, the present study systematically investigates the fatigue behavior of a ferrite-pearlite medium-strength wheel steel ($\sigma_u \approx$ 0.9 GPa) under rotating bending (RB, 52.5 Hz) and ultrasonic axial cycling (UAC, ~20 kHz) at stress ratios of $R = -1$ and 0.3. The combined use of micro/nano sampling and multi-scale microscopy techniques enabled direct observation of sulfide-governed crack initiation and stress-ratio-dependent microstructural evolution. Furthermore, the study establishes a probability-based framework to describe the failure distribution under different loading types and ratios. By doing so, it broadens current VHCF knowledge — traditionally centered on martensitic steels — and provides new insights into how inclusions, loading type, and mean stress jointly control the long-term durability of wheel steels. The present study therefore represents a step toward bridging the gap between laboratory fatigue testing and real-world wheel performance assessment.

2. Material and methods

2.1. Research approaches

For the purpose, as shown in Fig. 1, we outline the methodological process of fatigue testing and microstructural analysis for the wheel.

First, tensile and fatigue specimens were sampled from the wheel rim, perpendicular to its inner/outer plane. Second, the original rim microstructure was carefully examined by using OM and SEM. Third, tensile properties were obtained and fatigue tests were conducted over the range of 10^3 to 10^9 cycles under three different loading conditions: (1) RB, 52.5 Hz, $R = -1$; (2) UAC, ~ 20 kHz, $R = -1$; (3) UAC, ~ 20 kHz, $R = 0.3$. Fourth, S-N data and their fitted curves were plotted. Fifth, Haigh-type diagrams were employed to describe the effect of tensile mean stress under approximate infinite fatigue life. Sixth, detailed failure analysis was conducted on fatigue fracture surfaces under three loading conditions using SEM. Seventh, FIB sample preparations and TEM characterizations were performed on the crack initiation regions of typical VHCF specimens failed under UAC loading with different stress ratios, aiming to determine their microstructural characteristics.

Based on the results, we reveal fatigue characteristics of crack initiation and early growth from low-cycle to very-high-cycle regimes, discuss the effects of loading type and stress ratio, and finally evaluate the failure probability distribution.

2.2. Material and sampling

The material investigated is a high-carbon steel (CL60), defined as such according to a Chinese industry standard [61], with relatively lower carbon content (hypoeutectoid) and commonly used in high-speed railway applications. The chemical composition, as provided by the manufacturer (Taiyuan Heavy Machinery Group Co., Ltd., Taiyuan, Shanxi, China), is as follows (in weight percentage): 0.61C, 0.27Si, 0.65 Mn, <0.035 S, <0.035P, <0.25 Cr, <0.25 Ni, <0.25 Cu, with the balance being Fe. The railway wheel was shaped through hot forging to form the wheel blank and refine its grain structure, followed by tread surface quenching — typically via induction heating — to boost tread hardness and wear resistance, with a subsequent tempering step to alleviate residual stresses.

Sampling was conducted on a forged wheel segment extracted from the service stock. As shown in Fig. 2, the round bar used for specimen preparation was sampled 15 mm radially inward from the tread surface, with its axis perpendicular to both the inner and outer planes of the wheel rim. The extraction was performed along the wheel axis direction to retain the rolling and forging textures, and to capture the representative microstructural and residual stress states associated with wheel rim service conditions. The wheel rim location was specifically selected because it is one of the critical fatigue-sensitive regions in service due to the alternating bending and compressive contact stresses during wheel-rail interaction.

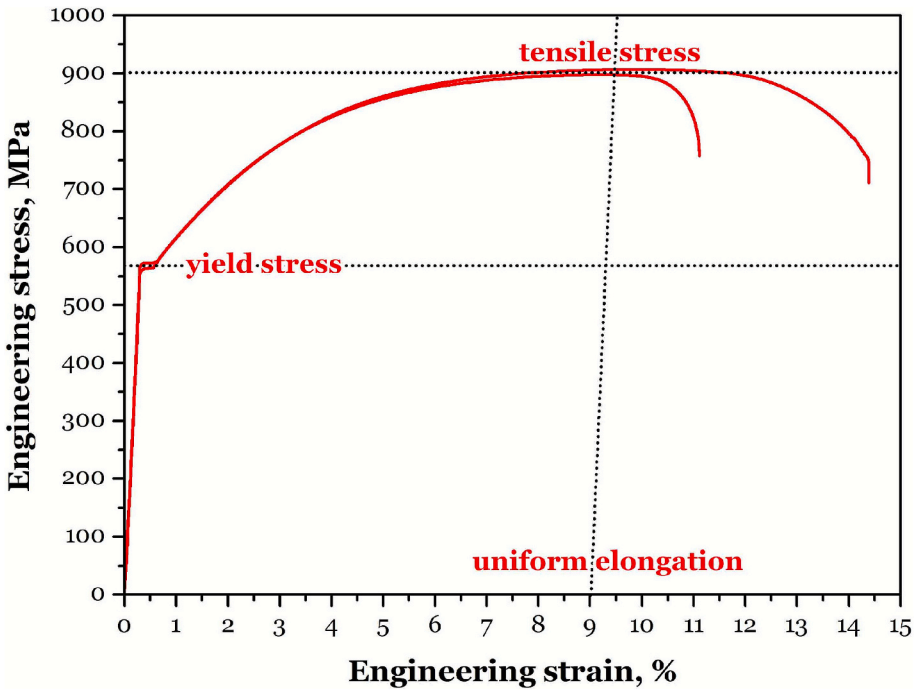

Fig. 5. Tensile curves of two specimens under monotonic quasi-static loading in ambient air at room temperature.

2.3. Specimens and testing

Three types of specimens were prepared to characterize the mechanical properties and fatigue behavior of the wheel rim under different loading types and stress ratios. Their geometries and dimensions are shown in Fig. 3.

In accordance with ASTM E8 standards [62], the monotonic tensile specimens (Fig. 3a) were machined to have a standard cylindrical geometry, with a shoulder diameter of 16 mm, gauge diameter of 6 mm, and gauge length of 40 mm. These tests were conducted using a servo-hydraulic testing machine (MTS Landmark 858, MTS Systems Corporation, Eden Prairie, MN, USA) under displacement control at a constant strain rate of $1 \times 10^{-3}\ s^{-1}$. Tests were performed at room temperature in ambient air, and extensometers were used to monitor the gauge section strain. Tensile tests were conducted primarily to determine the material's yield strength, UTS, and uniform elongation, which serve as reference properties for interpreting fatigue performance.

UAC fatigue specimens (Fig. 3b) featured an hourglass-shaped design, optimized for resonance at 20 ± 0.5 kHz, as reported in Refs. [21,22]. These specimens were employed for VHCF tests under axial loading conditions at stress ratios $R = -1$ and 0.3. Tests were carried out on an ultrasonic fatigue testing system (GF20-KT, LASUR, Asnières-sur-Seine, France), where sinusoidal excitation was applied via a piezoelectric actuator. Displacement amplitude was calibrated using strain gauges, and an active air-cooling system was used to ensure that specimen surface temperatures did not rise excessively during testing. For each test, failure was defined as the specimen's frequency decreasing sufficiently or fast enough to cause the device to stop resonating, while run-outs were defined as specimens surviving beyond 10^9 cycles without visible cracks. To evaluate mean stress effects, a separate set of specimens was tested at $R = 0.3$ by introducing a tensile static preload combined with UAC.

RB fatigue specimens (Fig. 3c) had a double-notch profile with a minimum diameter of 3.5 mm and a fillet radius of 7 mm, designed to further concentrate stress at the specimen surface, with a stress concentration factor of 1.07, as obtained from Ref. [63]. These tests were conducted at 52.5 Hz using a dual-spindle RB fatigue machine (GIGA-QUAD YRB200, YAMAMOTO, Osaka, Japan) under fully reversed loading conditions ($R = -1$). Each specimen was carefully balanced prior to testing to avoid dynamic misalignment and spurious vibrations.

2.4. Microscopy procedures

Before the sampling round bars described in § 2.1 were processed into the specimens in § 2.2, in accordance with Chinese standards [64], we cut them to prepare metallographic and microstructure observation specimens.

Since the wheel steel is a hypoeutectoid steel, a two-step etching sequence was employed to optimize phase contrast and reveal the morphologies of both ferrite and pearlite for samples observed under OM (Figs. 4a and b) using a Zeiss Axiovert 200 MAT (Carl Zeiss Microscopy GmbH, Jena, Germany). First, a 2 % Nital solution (2 vol% nitric acid in ethanol) was used to delineate the general microstructural framework, followed by LePera reagent, composed of picric acid and sodium metabisulfite in ethanol, which selectively stains ferrite and pearlite in contrasting tones. This combined approach enabled clear identification of equiaxed domains/grains and phase boundaries in both transverse and longitudinal sections, confirming the uniformity of the ferrite-pearlite matrix. In the OM images, the bright white areas correspond to ferrite domains, while the dark gray areas correspond to pearlite domains. Overall, the pearlite domains are equiaxed, whereas the ferrite domains exhibit irregular elongated shapes. No significant banding or textural anisotropy was observed, and microstructures oriented either perpendicular or parallel to the specimen axis showed no appreciable difference.

SEM manifests distinct contrast and higher spatial resolution compared to OM, traits particularly pronounced in field-emission SEM (FESEM). Leveraging these traits, we carried out more detailed observations on the microstructure of the wheel rim using a Zeiss Merlin FESEM (Carl Zeiss Microscopy GmbH, Jena, Germany). Fig. 4c shows the morphology of inclusions in the pearlite matrix. Our previous work [55] has confirmed that these inclusions are sulfides, which is consistent with descriptions in the literature [39,65,66]. Unlike oxides, sulfide inclusions are inherently soft, and thus tend to be deformed and elongated along with the matrix material during forging, exhibiting irregular elongated clusters. Fig. 4d shows the morphology and distribution

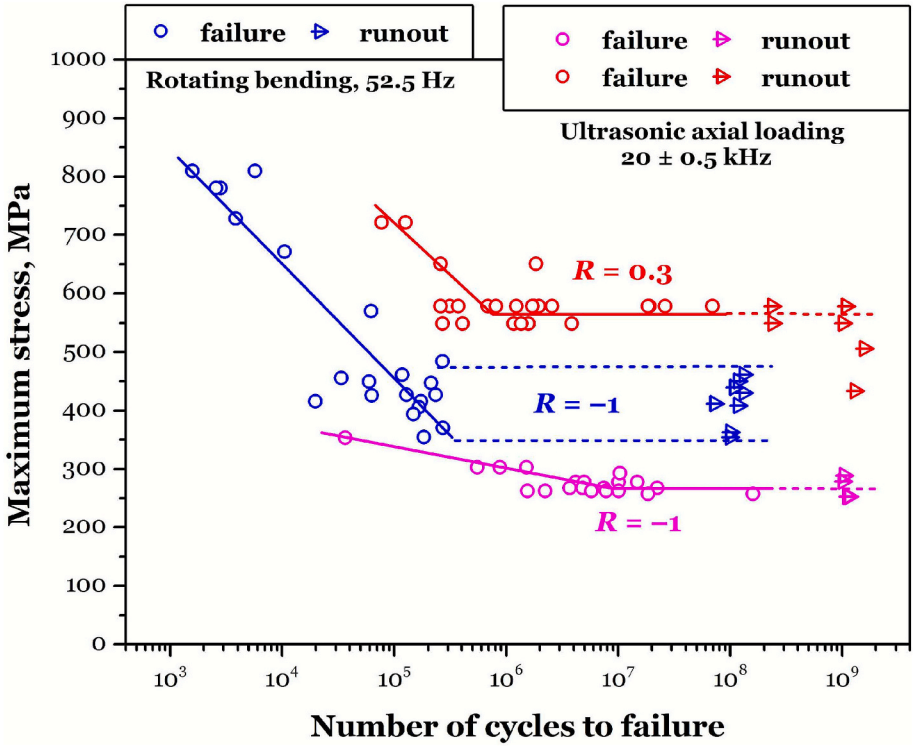

Fig. 6. S-N data and curves of different specimens under various loading conditions.

characteristics of pearlite and ferrite in the wheel rim, which is consistent with the OM results. No ferritic grains or their grain boundaries were observed. In literature [55], we statistically analyzed the grain size of wheel rim using electron backscatter diffraction (EBSD), showing that the size of the pearlite domains is in the range of 17 ± 6.2 μm, while the size of the ferrite domains is much smaller.

For the ultrasonic fatigue tests, some of the failed specimens had completely fractured, while others remained partially connected. To handle this, we used a tensile testing machine to fully fracture all specimens with visible cracks after UAC loading. For the RB fatigue tests, all failed specimens had completely fractured. In the case of these specimens, we carefully observed their fracture morphologies under a tungsten filament SEM (JEOL JSM-IT300, JEOL Ltd., Tokyo, Japan), selected locations near crack initiation sites on the fracture surfaces to prepare TEM samples using a FIB/SEM dual beam system, FEI Helios Nanolab 600i, and characterized them using two TEMs: FEI Tecnai G2 F20 and FEI Talos F200X. Note that the latter three instruments were all manufactured by FEI Company (Hillsboro, OR, USA), which has now been acquired by Thermo Fisher Scientific (Waltham, MA, USA).

3. Results and discussion

3.1. Tensile properties

Quasi-static tensile tests were conducted on the specimens at room temperature in ambient air to establish the reference mechanical properties of the wheel rim. The engineering stress–strain curves derived from these tests are presented in Fig. 5, with each curve corresponding to a specimen.

This wheel steel features a distinct yield plateau at $\sigma_y = 569$ MPa, a necking point at $\sigma_u = 901$ MPa, and a uniform elongation of $\delta_u = 9.0$ %, accompanied by stable work hardening and considerable ductility until final fracture. After necking, i.e. when the specimen enters the post-uniform deformation stage [67], the tensile plasticity exhibits a certain degree of dispersion, with the elongation after fracture δ_f being 10.7 % and 14.0 % respectively.

In contrast to traditional high-strength high-carbon steels, which have a martensitic microstructure and are regarded as having typical VHCF behavior [13,27,31], the wheel steel investigated in this paper demonstrates tensile properties analogous to those of low-carbon or medium-carbon steels. It has a distinct yield plateau, which is a typical characteristic of ferritic or pearlitic steels.

3.2. S-N data and Haigh diagrams

Fatigue tests were conducted under two distinct loading types — rotating bending (RB) and ultrasonic axial cycling (UAC) — to evaluate the fatigue performance of the wheel steel across a wide range of life regimes under three conditions: (1) RB loading from 10^3 to beyond 10^8 cycles for 29 tests, UAC loading from 3×10^4 to beyond 10^9 cycles for stress ratios of (2) $R = -1$ with 24 tests and (3) $R = 0.3$ with 31 tests. The corresponding S-N data and curves are shown in Fig. 6 in terms of maximum stress (σ_{max}) versus fatigue life (N_f, failure or runout), while Fig. 7 presents Haigh-type diagrams [68] in terms of both stress amplitude versus mean stress ($\sigma_a - \sigma_m$) and maximum stress versus mean stress ($\sigma_{max} - \sigma_m$) for the "infinite" fatigue life.

In Fig. 6, these three sets of S-N data have no overlap and are clearly distinguishable. Overall, when sorted by the values of maximum stress σ_{max} in descending order, they are as follows: UAC, $R = 0.3$; RB, $R = -1$; UAC, $R = -1$. Each of their S-N curves consists of a single sloped line and a horizontal asymptote. For the RB specimens, there are distinct upper and lower bounds for the horizontal asymptote: $\sigma_{max} = 351$ and 476 MPa; for the UAC specimens, the horizontal asymptotes are at $\sigma_{max} = 578$ and 266 MPa with $R = 0.3$ and -1. RB specimens either failed in the low-cycle or high-cycle fatigue stage corresponding to the first sloped line, or reached runout at approximately 10^8 cycles. None of the specimens failed in the horizontal asymptote region (i.e. $N_f > 3 \times 10^5$ cycles). When $R = -1$, no UAC specimens exhibited failure cycles exceeding 1.7×10^8; when $R = 0.3$, their failure cycles did not exceed 8×10^7. Although no VHCF failures were observed under RB loading, the actual service life of railway wheels can exceed $10^8 - 10^9$ cycles, where VHCF failures are indeed possible. The UAC results better represent this

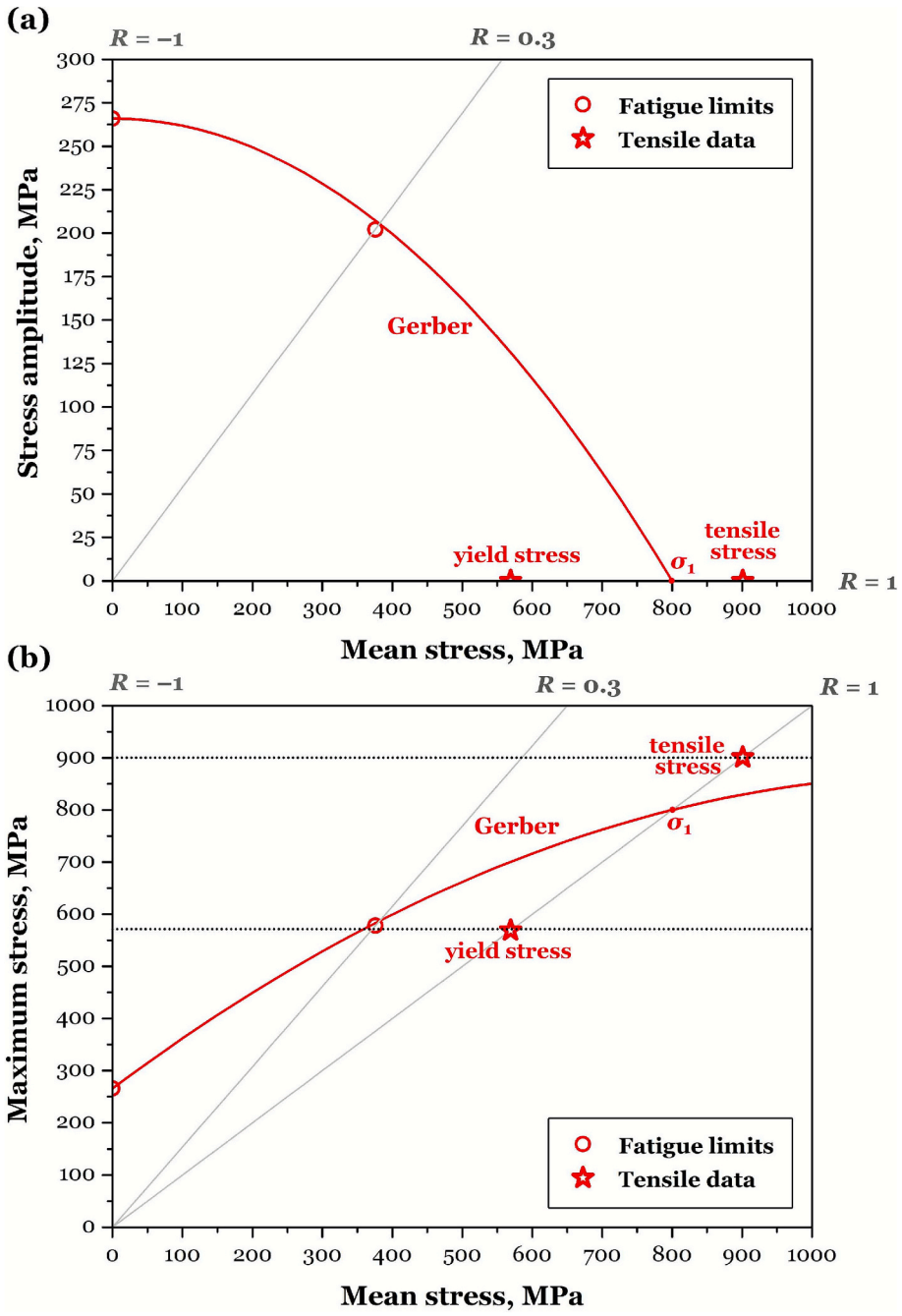

Fig. 7. Fatigue infinite-life contours: (a) stress amplitude σ_a versus mean stress σ_m, (b) maximum stress σ_{max} versus mean stress σ_m.

scenario, indicating that real wheels are at risk of inclusion-driven VHCF failures in long-term service.

In RB loading, even when the maximum stress σ_{max} attains 800 MPa, which is close to the UTS of the wheel steel, the specimens can still withstand a cyclic load of $1.59 - 5.72 \times 10^3$ cycles. This reflects the beneficial effect of strain or stress gradient: the maximum stress exists only in the outermost layer of the specimen; the deeper into the specimen interior, the smaller the actual load, which enables the specimen to resist a larger nominal load (i.e. the maximum stress σ_{max}). For RB specimens, there exists a "traditional" fatigue limit: under a same load, if a specimen does not fail at 10^7 cycles, it will not fail at 10^8 cycles or even longer cycles. At the same stress ratio of $R = -1$, RB specimens generally exhibit higher fatigue performance than the UAC ones. This can be attributed not only to the strain/stress gradient in RB loading but also to the harmful effect of loading frequency in UAC loading.

This result contradicts conventional understanding [29]: multiple experiments [13,27] have demonstrated that for medium- or low-strength steels, UAC loading tends to achieve higher strength than that under conventional frequencies; even with the benefit of strain gradients, its performance remains superior to that under RB loading. This is most likely because the gain in material strength induced by the high strain rate [13] from ultrasonic loading is less significant than the reduction in material strength caused by the temperature rise [56] it brings about. When under the same UAC loading condition, at $R = 0.3$, the fatigue resistance expressed by maximum stress is significantly enhanced, whether in high-cycle or very-high-cycle regime. As the stress ratio increases, the knee point of the S-N curve for UAC specimens shifts leftward from 9.2×10^6 cycles to 7.6×10^5 cycles, with the sloped segment becoming steeper. For RB loading, the knee point shifts further to 3×10^5 cycles, and the sloped segment becomes even steeper.

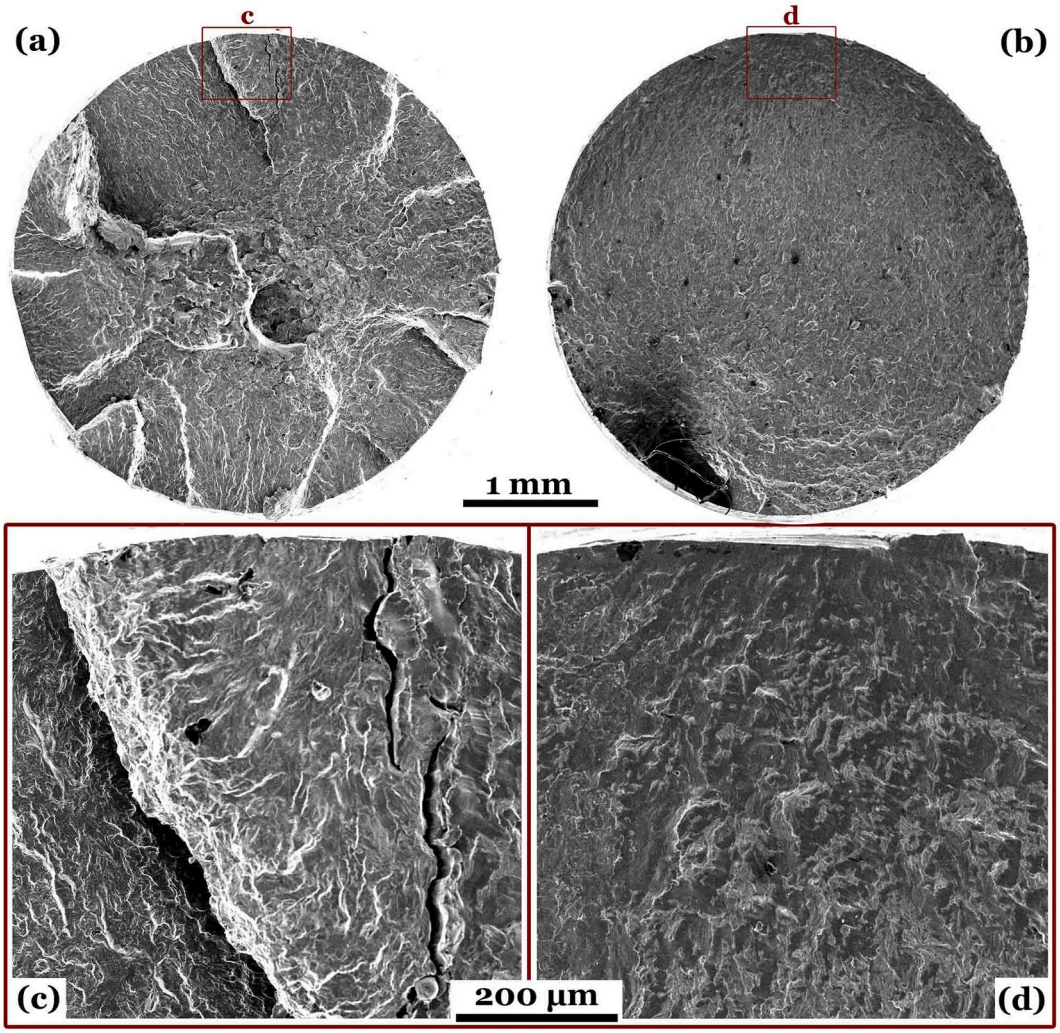

Fig. 8. Representative SEM images showing the whole fracture surfaces (a,b) and the enlarged boxes c,d for the crack initiation regions (c,d) in (a,b) of specimens under rotating bending ($R = -1$): (a,c) $\sigma_{max} = 416$ MPa, $N_f = 1.98 \times 10^4$ cycles; (b,d) $\sigma_{max} = 427$ MPa, $N_f = 2.33 \times 10^5$ cycles.

UAC specimens also exhibit a fatigue limit: at $R = -1$, near the horizontal asymptote of $\sigma_{max} = 266$ MPa, the specimens may fail before 1.7×10^8 cycles or remain intact even after 10^9 cycles; at $R = 0.3$, near the horizontal asymptote of $\sigma_{max} = 578$ MPa, the specimens may fail before 8×10^7 cycles or remain intact even after 10^9 cycles. Fig. 7 a and b plots the fatigue limit curves in terms of stress amplitude σ_a and maximum stress σ_{max} with increasing tensile mean stress σ_m on a Gerber [69] typed equation:

$$\frac{\sigma_a}{\sigma_{-1}} = 1 - \left(\frac{\sigma_m}{\sigma_1}\right)^2 \quad (1)$$

where σ_{-1} is the fatigue limit at $R = -1$, σ_1 is a tensile parameter for the wheel steel. When σ_1 is taken as σ_u, the expression degenerates into the Gerber relation [69]. Therefore, σ_1 can be regarded as a fatigue limit at $R = 1$. In Fig. 7, with σ_1 set to 800 MPa, Eq. (1) can well describe the fatigue limits under stress ratios $R = -1$ and 0.3. In the present analysis, σ_1 was set to 800 MPa, which lies between the yield strength ($\sigma_y = 569$ MPa) and the UTS ($\sigma_u = 901$ MPa) of the wheel steel. This choice reflects the physical constraint that at high mean stresses, the fatigue limit should not exceed the stress level at which plastic yielding occurs. Therefore, σ_1 can be regarded as an effective limiting stress parameter that bridges the fatigue limit at $R = -1$ and the yielding-dominated regime at high mean stress. The selected value of 800 MPa not only achieves good agreement with the experimental data but also maintains consistency with the Gerber-type relation and the tensile properties of ferrite-pearlite steels.

For cases with high stress ratios ($R > 0.3$), the extrapolated fatigue limit curves may not be reliable due to the lack of experimental data. However, for the stress ratio range from $R = -1$ to $R = 0.3$, the results should have a relatively high confidence level. Fig. 7b shows that the maximum stress corresponding to the fatigue limit at $R = 0.3$ is comparable to the yield strength of the wheel steel, indicating the regulatory role of the yield strength under such loading conditions. Schönbauer et al. [70] reported similar findings, further emphasizing the sensitivity of pearlitic and ferritic steels with $\sigma_u < 1$ GPa to tensile mean stress [71]. This also indicates that attempting to quickly estimate fatigue strength using a single UTS, particularly for VHCF, is inherently futile [72].

At the same stress ratio of $R = -1$, RB specimens generally exhibited higher fatigue performance than the UAC ones. This result appears to contradict conventional understanding, since many studies [13,27,29] have reported that ultrasonic loading tends to enhance fatigue resistance compared with conventional frequencies, particularly in high-strength steels. The discrepancy can be explained by the loading frequency effect and the associated thermal influence. At ultrasonic frequency (~ 20 kHz), the high strain rate is expected to provide a strengthening effect by delaying plastic instability. However, in the present wheel steel with $\sigma_u \approx 0.9$ GPa, this potential benefit is outweighed by thermal softening. Despite active air cooling, local heating is unavoidable in ultrasonic tests, particularly near elongated sulfides where stress concentration

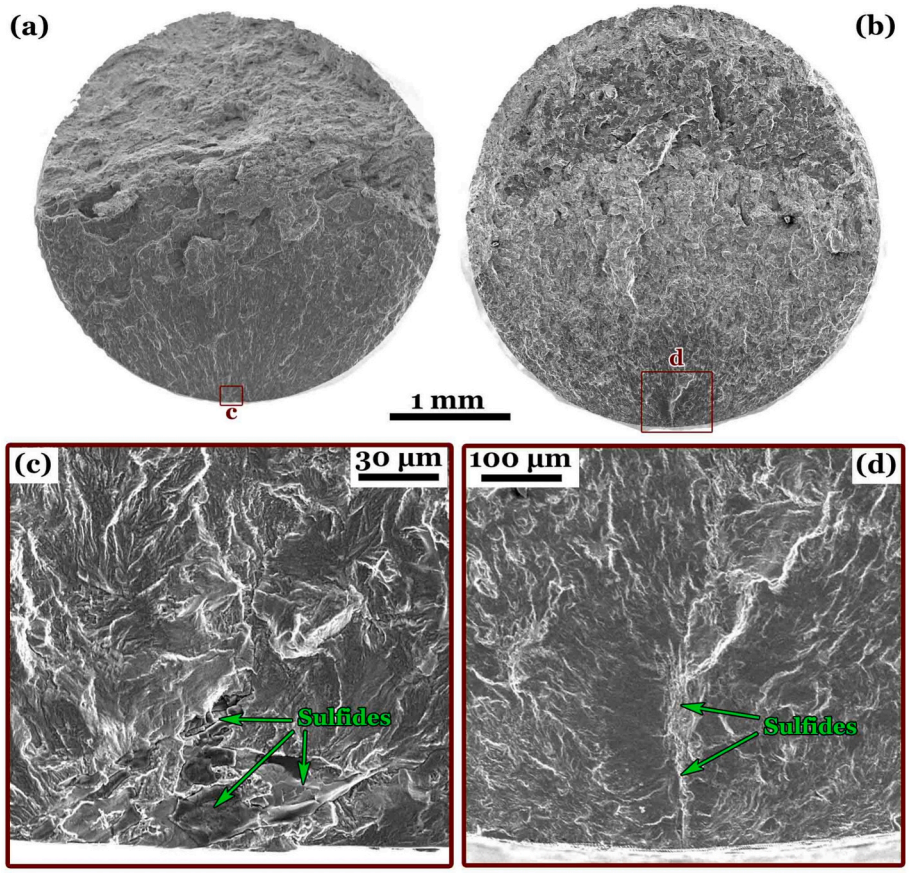

Fig. 9. Representative SEM images showing the whole fracture surfaces (a,b) and the enlarged boxes c,d for the crack initiation regions (c,d) in (a,b) of specimens under ultrasonic axial loading ($R = -1$): (a,c) $\sigma_{max} = 304$ MPa, $N_f = 5.50 \times 10^5$ cycles; (b,d) $\sigma_{max} = 268$ MPa, $N_f = 3.70 \times 10^6$ cycles.

and cyclic plasticity are severe. The temperature rise was controlled to remain below ~ 30 °C at the specimen surface, yet even moderate heating can promote partial dissolution of cementite lamellae and reduce resistance to crack initiation. Consequently, the fatigue resistance under UAC is significantly lower than under RB loading, in contrast to conventional understanding for high-strength steels. This highlights that the frequency effect is strongly coupled with material strength level and microstructural sensitivity: in medium strength steels, thermal damage dominates over strain-rate strengthening. From an engineering perspective, this implies that ultrasonic fatigue testing provides a conservative but realistic assessment of inclusion-driven VHCF risks for railway wheels in long-term service.

3.3. Fracture surface morphologies

Fractographic examination was performed to investigate crack initiation locations and surface morphologies under different loading types and stress ratios. Fracture features are strongly dependent on both the stress state (RB vs. UAC loading) and the stress ratio level ($R = -1$ vs. 0.3). A systematic shift was observed from surface-initiated cracks under RB loading to subsurface or internal crack initiation under UAC loading. Representative SEM images of fracture surfaces are presented in Figs. 8–10, covering the full range of loading scenarios.

For RB loading, a total of 21 specimens failed, all of which were dominated by surface crack initiation and corresponded to low-cycle or HCF. Two examples are presented in Fig. 8: one involves multiple initiation sites (Fig. 8a) with a relatively low number of failure cycles (1.98×10^4), and the other is a single initiation site (Fig. 8b) with a relatively high number of failure cycles (2.33×10^5). Note: The load applied to the specimen corresponding to Fig. 8a ($\sigma_{max} = 416$ MPa) is slightly less than that for Fig. 8b ($\sigma_{max} = 427$ MPa). In both cases of Fig. 8 a and b, concentric crack propagation bands are clearly visible, indicating stable fatigue crack growth. Enlarged views of the crack initiation sites (Fig. 8 c and d) reveal smooth, shallow features free of noticeable inclusions or voids, suggesting that the fatal fatigue damage was governed by the specimen surface condition and/or microstructure rather than inclusion or void typed defects. We define this type of fatigue failure, which is dominated by the specimen surface and involves no inclusions, as the "Sur-1" (surface without inclusions).

For UAC loading, a total of 21 specimens failed at $R = -1$, with 25 specimens failing at $R = 0.3$. The representative SEM morphologies of the fracture surfaces (Figs. 9 and 10) show that these failed specimens are dominated by either internal or surface crack initiation. The influence of stress ratio on fractographic features appears to be relatively minor, at least for R values of 0.3 and –1. Unlike the failed specimens under RB loading, the fatigue fracture surfaces of UAC specimens all exhibit inclusion-induced crack initiation; these inclusions, after identification, are confirmed to be sulfides [55]. Based on fractographic knowledge [73], we first determine whether a fracture surface originates from a surface crack or an internal crack. Depending on the positions of the dominant sulfide inclusions, and with reference to the illustration in Ref. [74], we have defined two other failure types: "Sur-2" (surface with inclusions, as shown in Figs. 9a,c and 10a,c) and "Int" (interior with inclusions, as shown in Figs. 9b,d and 10b,d).

Under $R = -1$, Fig. 9 a and c presents an example of Sur-2 typed failure, while Fig. 9 b and d presents an example of Int typed failure. Fig. 9a shows a typical fracture surface dominated by surface-initiated failure in low-cycle or HCF, with a failure cycle count on the order of 10^5. Fig. 9b demonstrates a somewhat non-standard FiE morphology, which, strictly speaking, corresponds to subsurface-initiated failure,

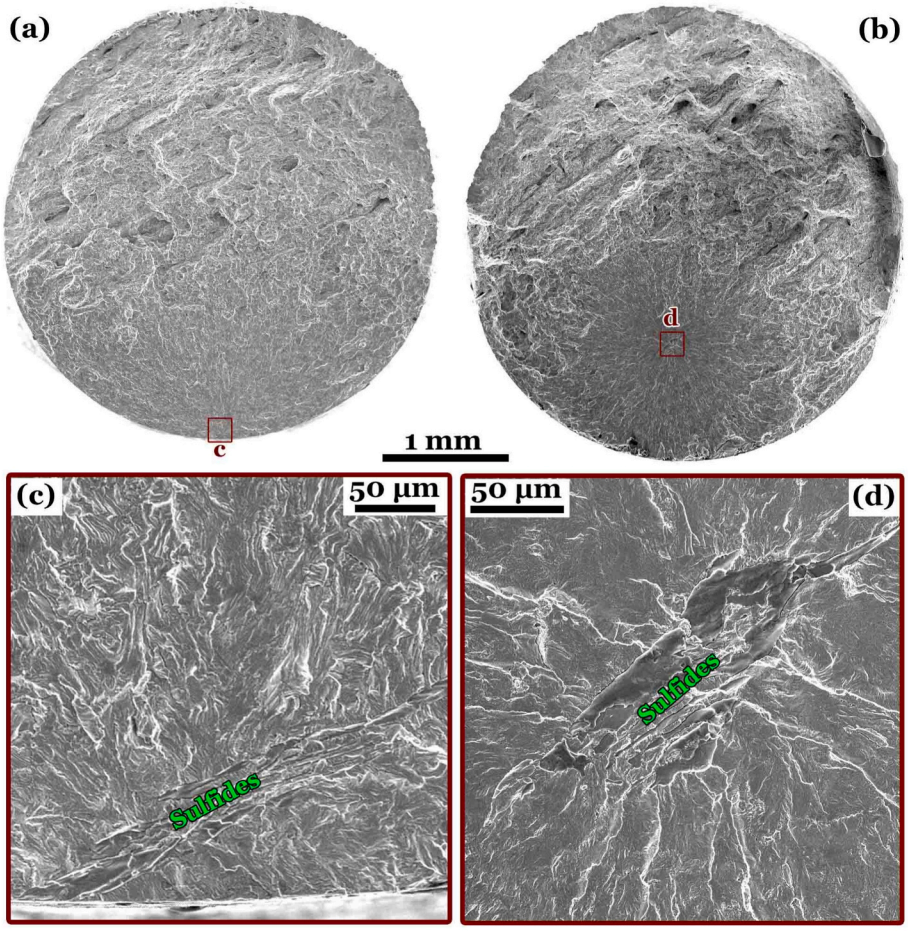

Fig. 10. Representative SEM images showing the whole fracture surfaces (a,b) and the enlarged boxes c,d for the crack initiation regions (c,d) in (a,b) of specimens under ultrasonic axial loading ($R = 0.3$): (a,c) $\sigma_{max} = 578$ MPa, $\sigma_a = 202$ MPa, $N_f = 1.23 \times 10^6$ cycles; (b,d) $\sigma_{max} = 578$ MPa, $\sigma_a = 202$ MPa, $N_f = 1.84 \times 10^7$ cycles.

with a failure cycle count on the order of 10^6. The enlarged SEM image of Fig. 9c exhibits the fragmented sulfide clusters in the surface crack origin of the specimen, with sizes in the range of 60 – 100 μm. Fig. 9d magnifies the morphology of the subsurface crack initiation region in Fig. 9b, where a long serpentine domain containing sulfide inclusions divides the indistinct elliptical FiE region into two parts. This elongated sulfide domain has a major axis of approximately 300 μm and a minor axis of about 50 μm.

Under $R = 0.3$, Fig. 10 a and c presents an example of Sur-2 typed failure, while Fig. 10 b and d presents an example of Int typed failure. Fig. 10a is very similar to Fig. 9a, both showing the typical fracture surface morphology under surface crack initiation in HCF, though with a failure cycle count on the order of 10^6. In contrast, Fig. 10b presents a standard FiE fracture of VHCF dominated by internal crack initiation, featuring a failure cycle count on the order of 10^7. Fig. 10 c and d displays the morphology of dominant sulfide inclusions in the initiation region. These inclusions are all in the form of elongated ellipsoidal or long strip-like shapes, with their major axes each around 300 μm and their minor axes measuring 30 and 60 μm.

In comparing Figs. 10d and 9d, it is confirmed that the internal FiE origins appear smooth and inclusion-associated, yet exhibit more distinct radial growth patterns at $R = 0.3$ than those of the $R = -1$ case. The presence of tensile mean stress likely promotes crack opening, mitigates crack closure effects, and facilitates the faster growth of internally initiated cracks, thereby shifting the failure mechanism from surface-, subsurface- to internal-initiated even at high maximum stress levels.

From an engineering viewpoint, although all RB specimens failed by surface crack initiation, the actual wheel rim is more realistically represented by the UAC results. In service, wheels are subjected to complex bending and rolling-contact stresses in a large volume, where elongated sulfide inclusions are inevitably present. Therefore, fatigue failures in real wheels are expected to be dominated by sulfide-induced mechanisms, which can occur both at the surface and in the interior depending on the state of the local stress.

3.4. Crack initiated micro/nanostructure

Compared with the VHCF of high-strength steels [7,19,33] with a tempered martensite, the failure lives of RB and UAC specimens for the wheel steel are not particularly high, nor have we observed morphological features such as ODA or FGA in the crack initiation regions. Nevertheless, we still used the FIB technique to prepare longitudinal cross-sectional samples of the pearlite-ferrite matrix along the edges of sulfide inclusions that induce crack initiation, for subsequent TEM characterization. The fracture surfaces of selected specimens are shown in Fig. 11 a and b, corresponding respectively to the UAC loading conditions as follows: (1) $R = -1$, $\sigma_{max} = 278$ MPa, $\sigma_a = 278$ MPa, $N_f = 1.01 \times 10^7$ cycles; (2) $R = 0.3$, $\sigma_{max} = 578$ MPa, $\sigma_a = 202$ MPa, $N_f = 2.62 \times 10^7$ cycles.

We conducted site-specific TEM analyses on the two thin foils, denoted as the red bars c and d in Fig. 11 a and b, which mark the FIB locations on the fracture surfaces. The bright field (BF) images are shown in Fig. 11 c and d for two TEM samples. For $R = -1$, there are two distinct microstructural zones: near the fracture surface lies a layer of ultrafine equiaxed ferrite grains with sizes ranging from hundreds of

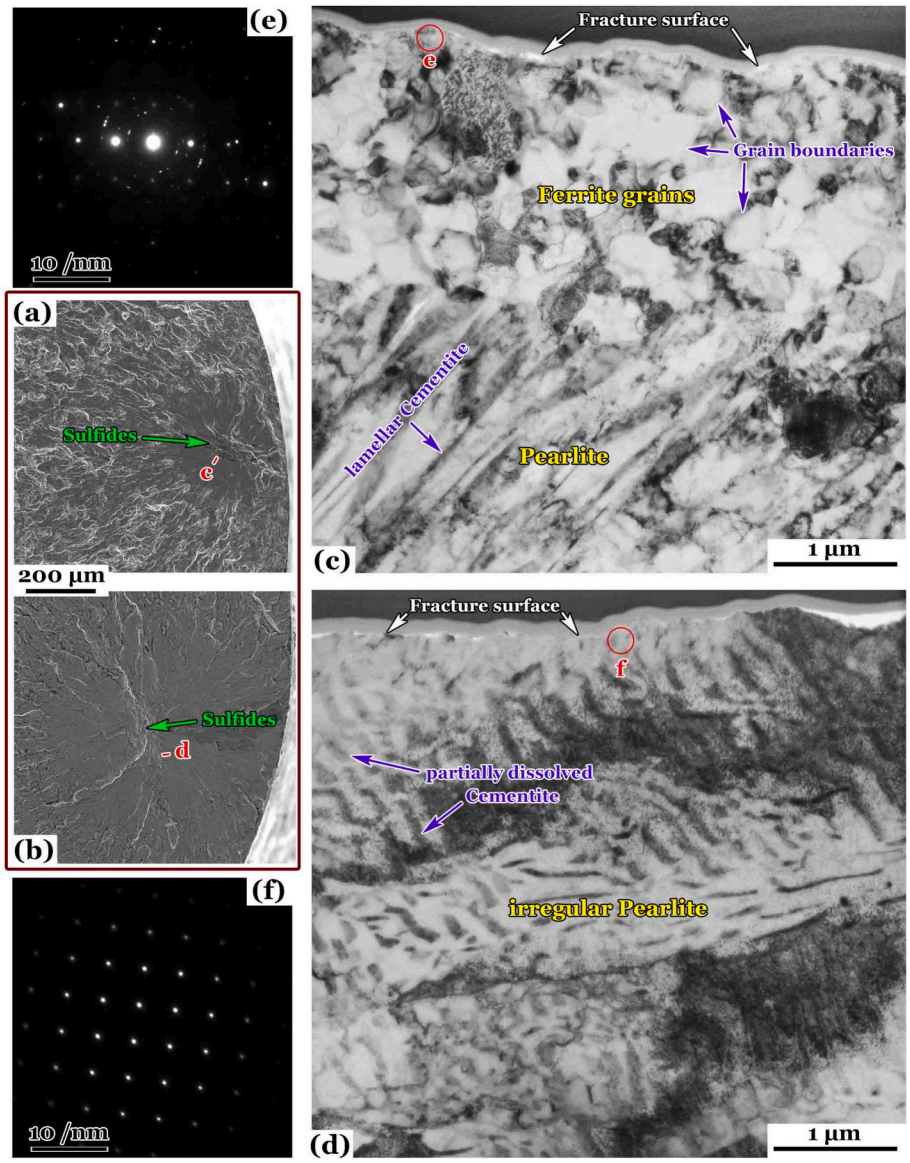

Fig. 11. Representative FiE morphologies under SEM of two ultrasonic specimens failed in VHCF regime at negative and positive stress ratios: (a) $R = -1$, $\sigma_{max} = 278$ MPa, $\sigma_a = 278$ MPa, $N_f = 1.01 \times 10^7$ cycles; (b) $R = 0.3$, $\sigma_{max} = 578$ MPa, $\sigma_a = 202$ MPa, $N_f = 2.62 \times 10^7$ cycles. Red bars c,d in (a,b) indicating TEM sampling locations by FIB milling. (c,d) BF images for TEM samples c,d; (e,f) SAD patterns for e,f domains in (c,d); respectively.

nanometers to sub-microns; away from the fracture surface, there is a conventional pearlite region, where the ferritic lamellae have a thickness of approximately 200 nm, and the cementite lamellae have a thickness of less than 100 nm. In comparison with the proeutectoid ferrite grains in the original ferrite-pearlite microstructure, their sizes appear to have undergone significant refinement. Very recently, Sistaninia et al. [75] also observed a similar phenomenon of ferrite grain refinement during VHCF loading in R350HT, a pearlitic steel commonly used in Europe, with the key difference that no sulfide inclusions were detected therein. For $R = 0.3$, there is only a microstructure consisting of irregular pearlite, in which partially dissolved cementite can be observed. The pearlite regions have a size exceeding the observable range of the TEM sample, and thus no obvious grain refinement is detected.

As shown in the BF images of Fig. 11 c and d, the red circles, each with a diameter of 200 nm, located near the fracture surfaces, marked as e and f, are representative domains for selected area electron diffraction (SAD), with their characterization results presented in Fig. 11 e and f. The SAD pattern in Fig. 11e exhibits disordered diffraction spots, with faintly elongated rings visible locally — a feature indicative of a high density of randomly oriented nanograins, which suggests severe cyclic plasticity and microstructural fragmentation at the VHCF crack origin. This indicates that under the VHCF condition with $R = -1$, where the failure cycle number of the wheel steel is not particular high, only a discontinuous and very thin nanocrystalline layer exists in the core region of fatigue crack initiation. Unlike the $R = -1$ condition, the SAD pattern in Fig. 11f reveals isolated diffraction spots, indicating the presence of coarse pearlite lamellae larger than 200 nm in size after a VHCF loading under the $R = 0.3$ condition. The NCP (numerous cyclic pressing) model proposed by Hong et al. [34] can well account for these distinct microstructural characteristics in the crack initiation region of VHCF under such negative and positive stress ratios.

For the case of $R = -1$, Ref. [42] reported a phenomenon of aluminium grain refinement occurring in the crack initiation region of an additively manufactured AlSi10Mg after more than 4×10^8 cycles, which is highly similar to the ultrafine ferrite grains in Fig. 11c and is believed to be related to dynamic recrystallization. In addition, Ref. [56] also documented a significant refinement of ferrite grains in the crack

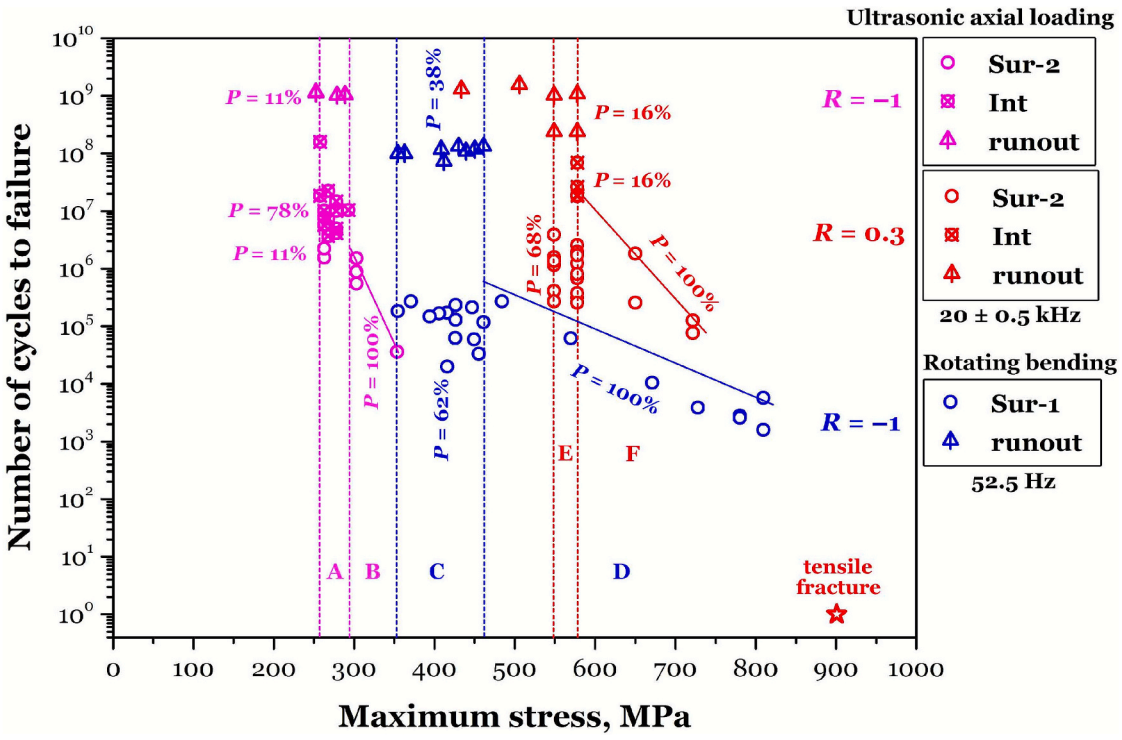

Fig. 12. N-S diagram showing failure probability under different loading conditions in terms of maximum stress.

initiation region of a ferrite-pearlite steel under VHCF with $R = -1$. The partial dissolution of cementite in Fig. 11d is likely related to both temperature and load. It is reasonable to infer that cementite dissolution also occurs near the fracture surface in Fig. 11c, which manifests as the dissolution, precipitation, and rearrangement of eutectic silicon in the additively manufactured aluminium alloy endured VHCF loading [42]. Furthermore, phase transformations such as those of retained austenite [76] are also highly likely to have intensified these microstructural evolution processes.

3.5. Failure types and their probabilities

Based on post-mortem fractographic inspection, we broadly categorize the failure types as follows: "Sur-1" (surface without inclusions), "Sur-2" (surface with inclusions) and "Int" (interior with inclusions). This classification applied to RB loading with σ_{max} ranging from 809 to 354 MPa, and to UAC loading with σ_{max} ranging from 354 to 258 MPa at $R = -1$, as well as from 722 to 549 MPa at $R = 0.3$. Following the method in Ref. [30], the S-N diagram (Fig. 6) can be transposed into an N-S diagram, and a failure phase map is thereby plotted, as shown in Fig. 12.

In Fig. 12, we also added the UTS to the horizontal axis. When $\sigma_{max} = \sigma_u$, the specimen fractures instantaneously, and its failure cycle number is defined as $N_f = 1$ or 10^0. For the three loading conditions listed in this paper, the runout data are distinctly separated from those of Sur-1, Sur-2, and Int. Among them: RB loading only induces Sur-1 failure, which is located in the middle-right part of the phase map; under the applied loads specified in this paper, UAC loading results solely in Sur-2 and Int failures, with the loading cycles required for Int failure consistently exceeding those for Sur-2. In the failure phase map, the negative and positive stress ratios of UAC loading are respectively distributed on the left and right sides of RB loading.

Under RB loading, the strain or stress gradient causes only the outermost layer of the specimen to be in the maximum stress state. If the V_{90} control volume [20,77] is defined by taking 90 % of this maximum stress value, its depth is only 175 μm, which can be comparable to the major axis length of the elongated sulfide-inclusion clusters in the steel. Therefore, in the V_{90} control volume (i.e. the outermost surface layer) of RB specimens, it is often difficult to encounter the sulfide inclusions with appropriate orientations. Furthermore, even if such inclusions exist, the driving force for cracking along the interface is easily suppressed by the strain gradient due to the strong coordinated deformation ability between MnS [55,78,79] and the matrix. In this way, the fatigue strength obtained from RB loading are significantly higher, which is determined by the combined effects of loading strain gradient and specimen size effect [13,77,80]. When applying this data, attention should be paid to it and corrections should be made accordingly.

Under UAC loading, the notch effect of the hourglass specimen is negligible, and its V_{90} control volume is 2 – 3 orders of magnitude higher than that of the RB specimen. Owing to the stress concentration around sulfide inclusions, combined with the lack of a sufficiently large strain gradient to inhibit crack initiation, all failed specimens tend to nucleate at the inclusion edges. Therefore, all failure types of the UAC specimens are dominated by sulfide inclusions. Consistent with the VHCF characteristics of traditional high-strength ($\sigma_u > 1.5$ GPa) steels [18,19,31], as the failure life increases, the initiation of fatal cracks shifts from inclusions on the specimen surface (Sur-2) to those in the specimen interior (Int).

For UAC loading, in contrast with the case of $R = -1$ and 0.3, it is easy to calculate that the occurrence probability of Int typed failure decreases from 78 % to 16 %, and the range of maximum stress is also significantly narrowed, from sub-domains A to E. More specifically, in sub-domain E, we only applied two loads, i.e. $\sigma_{max} = 549$ and 578 MPa. If calculated using this specific maximum stress, the occurrence probability of Int typed failure is 24 % at 578 MPa and 0 at 549 MPa. This is still much lower than that when $R = -1$, and the range where Int failure can occur is even smaller. The energy-based fatigue governing equation proposed in Ref. [42] can well explain this change: The pearlite disintegration, cementite dissolution, precipitation, and rearrangement, along with ferrite grain refinement and recrystallization, which accompany the process of crack initiation and early growth in Int typed failure, all consume a large amount of input cyclic strain energy. This enables the material to tolerate internal-origin failures within a wider range of

maximum stress or stress amplitude. These findings reinforce the view that crack initiation and early growth, with nanograin formation and microstructure refinement, constitute a generic feature [11,67] of VHCF, even in metallic materials with moderately low UTS values, such as the wheel steel investigated herein.

From an engineering perspective, these results emphasize that RB testing tends to overestimate the fatigue performance of wheel steels, since the effective control volume is too small for elongated sulfides to dominate. In contrast, UAC testing, with its much larger control volume, more realistically reflects service conditions by capturing inclusion-induced failures and their probability distribution. The pronounced decrease in interior failures under positive mean stress further indicates that wheel steels in service are more prone to surface-initiated fatigue at elevated mean stress levels, while the risk of internal VHCF failure becomes significantly reduced.

4. Conclusions

This study systematically investigated the fatigue behavior from low-cycle, high-cycle to very-high-cycle regimes of a wheel steel sampling from the wheel rim, with a ferritic-pearlitic microstructure, under rotating bending (RB) and ultrasonic axial cycling (UAC) with varying stress ratios of $R = -1$ and 0.3. The main findings are:

(1) RB specimens exhibited only surface-initiated failures and did not extend into the VHCF regime, whereas UAC specimens showed inclusion-induced failures (surface and interior) across high-cycle and very-high-cycle regimes.

(2) Due to strain/stress gradients and limited control volume, RB tests overestimate fatigue performance, while UAC tests more realistically capture inclusion-driven failures, highlighting the conservative but practical relevance of UAC for wheel steels.

(3) Microstructural investigations revealed nanograin formation and refinement under $R = -1$, and cementite dissolution under $R = 0.3$, demonstrating distinct mechanisms of crack initiation influenced by stress ratio and local thermal effects.

(4) Probability-based failure mapping shows that internal failures become significantly less frequent at positive stress ratios, indicating that service wheels are more prone to surface-initiated failures under tensile mean stresses.

CRediT authorship contribution statement

Hang Su: Writing – original draft, Visualization, Investigation. **Lu Liu:** Resources, Investigation, Funding acquisition, Data curation. **Runjie Yang:** Writing – original draft, Investigation, Formal analysis. **Zhiying Chen:** Investigation. **Shengnan Wang:** Supervision, Resources, Project administration. **Qing Peng:** Supervision, Resources, Project administration. **Xiangnan Pan:** Writing – review & editing, Writing – original draft, Visualization, Supervision, Resources, Project administration, Methodology, Investigation, Formal analysis, Conceptualization.

Declaration of competing interest

The authors declare that they have no known competing financial interests or personal relationships that could have appeared to influence the work reported in this paper.

Acknowledgments

This work was financially supported by Research fund of Xi'an Aeronautical University (Grant number: 2019KY1120) and Science Fund for Creative Research of Xi'an Aerospace Propulsion Institute (Grant number: 2025 Da.YY4006Da).

Dr. Xiangnan Pan sincerely extends his gratitude to Mr. Leiming Du — formerly a jointly supervised master's student at Harbin Institute of Technology, Shenzhen, with co-training at Institute of Mechanics, Chinese Academy of Sciences, and who graduated with his master's degree in 2021 — for his contributions to this work. Currently pursuing a Ph.D. degree at Delft University of Technology, Mr. Du's contributions primarily span the domains of "Data Curation, Investigation, and Resources."

Data availability

Data will be made available on request.

References

[1] Bathias C. There is no infinite fatigue life in metallic materials. Fatigue Fract Eng Mater Struct 1999;22(7):559–65. https://doi.org/10.1046/j.1460-2695.1999.00183.x.
[2] Sakai T. Review and prospects for current studies on very high cycle fatigue of metallic materials for machine structural use. J Solid Mech Mater Eng 2009;3:425–39. https://doi.org/10.1299/jmmp.3.425. in Japanese.
[3] Hong Y, Sun C. The nature and the mechanism of crack initiation and early growth for very-high-cycle fatigue of metallic materials – an overview. Theor Appl Fract Mech 2017;92:331–50. https://doi.org/10.1016/j.tafmec.2017.05.002.
[4] Jeddi D, Palin-Luc T. A review about the effects of structural and operational factors on the gigacycle fatigue of steels. Fatigue Fract Eng Mater Struct 2018;41(5):969–90. https://doi.org/10.1111/ffe.12779.
[5] Furuya Y, Shimamura Y, Takanashi M, Ogawa T. Standardization of an ultrasonic fatigue testing method in Japan. Fatigue Fract Eng Mater Struct 2022;45(8):2415–20. https://doi.org/10.1111/ffe.13727.
[6] Gao C, Zhang Y, Jiang J, Fu R, Du L, Pan X. Research viewpoint on performance enhancement for very-high-cycle fatigue of Ti-6Al-4V alloys via laser-based powder bed fusion. Crystals 2024;14(9):749. https://doi.org/10.3390/cryst14090749.
[7] Atrens A, Hoffelner W, Duerig T, Allison J. Subsurface crack initiation in high cycle fatigue in Ti-6Al-4V and in a typical martensitic stainless steel. Scripta Metall 1983;17(5):601–6. https://doi.org/10.1016/0036-9748(83)90385-X.
[8] Chang Y, Pan X, Zheng L, Hong Y. Microstructure refinement and grain size distribution in crack initiation region of very-high-cycle fatigue regime for high-strength alloys. Int J Fatigue 2020;134:105473. https://doi.org/10.1016/j.ijfatigue.2020.105473.
[9] Pan X, Qian G, Wu S, Fu Y, Hong Y. Internal crack characteristics in very-high-cycle fatigue of a gradient structured titanium alloy. Sci Rep 2020;10:4742. https://doi.org/10.1038/s41598-020-61484-3.
[10] Pan X, Xu S, Qian G, Nikitin A, Shanyavskiy A, Palin-Luc T, et al. The mechanism of internal fatigue-crack initiation and early growth in a titanium alloy with lamellar and equiaxed microstructure. Mater Sci Eng A-Struct 2020;798:140110. https://doi.org/10.1016/j.msea.2020.140110.
[11] Pan X, Su H, Liu X, Hong Y. Multi-scale fatigue failure features of titanium alloys with equiaxed or bimodal microstructures from low-cycle to very-high-cycle loading numbers. Mater Sci Eng A-Struct 2024;890:145906. https://doi.org/10.1016/j.msea.2023.145906.
[12] Xu S, Pan S, Li Z, Li S, He X, Pan X. Anisotropic tensile behavior and fracture characteristics of an additively manufactured nickel alloy without and with a heat treatment of solution aging. Mater Sci Eng A-Struct 2025;927:148015. https://doi.org/10.1016/j.msea.2025.148015.
[13] Hu Y, Sun C, Xie J, Hong Y. Effects of loading frequency and loading type on high-cycle and very-high-cycle fatigue of a high-strength steel. Materials 2018;11(8):1456. https://doi.org/10.3390/ma11081456.
[14] Naito T, Ueda H, Kikuchi M. Observation of fatigue fracture surface of carburized steel. J Soc Mater Sci 1983;32:1162–6. https://doi.org/10.2472/jsms.32.1162. in Japanese.
[15] Naito T, Ueda H, Kikuchi M. Fatigue behavior of carburized steel with internal oxides and nonmartensitic microstructure near the surface. Metall Trans A 1984;15:1431–6. https://doi.org/10.1007/BF02648572.
[16] Wöhler A. Bericht über die Versuche, welche auf der Königl. Niederschlesisch-Märkischen Eisenbahn mit Apparaten zum Messen der Biegung und Verdrehung von Eisenbahnwagen-Achsen während der Fahrt, angestellt wurden. Zeitschrift für Bauwesen 1858;8:642–52.
[17] Wöhler A. Versuche zur Ermittlung der auf die Eisenbahnwagen-Achsen einwirkenden Kräfte und der Widerstandsfähigkeit der Wagen-Achsen. Zeitschrift für Bauwesen 1860;10:548–616.
[18] Murakami Y, Nomoto T, Ueda T. Factors influencing the mechanism of superlong fatigue failure in steels. Fatigue Fract Eng Mater Struct 1999;22(7):581–90. https://doi.org/10.1046/j.1460-2695.1999.00187.x.
[19] Sakai T, Sato Y, Oguma N. Characteristic S-N properties of high-carbon-chromium-bearing steel under axial loading in long-life fatigue. Fatigue Fract Eng Mater Struct 2002;25(8–9):765–73. https://doi.org/10.1046/j.1460-2695.2002.00574.x.
[20] Murakami Y. Metal Fatigue: effect of Small Defects and Nonmetallic Inclusions. Oxford, UK: Elsevier; 2002.
[21] C. Bathias P. Paris Gigacycle Fatigue in Mechanical Practice 2005 Marcel Dekker New York, NY, USA 10.1201/9780203020609.
[22] Pan X. PhD Thesis: the research on the behavior of crack initiation and early growth in high-cycle and very-high-cycle fatigue regimes for titanium alloys. Beijing, China: University of Chinese Academy of Sciences; 2020. in Chinese.

[23] Sakai T. Historical review and future prospect for researches on very high cycle fatigue of metallic materials. Fatigue Fract Eng Mater Struct 2023;46(4):1217–55. https://doi.org/10.1111/ffe.13885.

[24] Y. Lee J. Pan R. Hathaway M. Barkey Fatigue Testing and Analysis: Theory and Practice 2005 Elsevier Butterworth-Heinemann New York, NY, USA 10.1016/B978-0-7506-7719-6.X5000-3.

[25] Willertz LE. Ultrasonic fatigue. Int Met Rev 1980;25(2):65–78. https://doi.org/10.1179/imtr.1980.25.1.65.

[26] Ebara R. The present situation and future problems in ultrasonic fatigue testing — mainly reviewed on environmental effects and materials' screening. Int J Fatigue 2006;28(11):1465–70. https://doi.org/10.1016/j.ijfatigue.2005.04.019.

[27] Zhao A, Xie J, Sun C, Lei Z, Hong Y. Effects of strength level and loading frequency on very-high-cycle fatigue behavior for a bearing steel. Int J Fatigue 2012;38:46–56. https://doi.org/10.1016/j.ijfatigue.2011.11.014.

[28] Fitzka M, Schönbauer BM, Rhein RK, Sanaei N, Zekriardehani S, Tekalur SA, et al. Usability of ultrasonic frequency testing for rapid generation of high and very high cycle fatigue data. Materials 2021;14(9):2245. https://doi.org/10.3390/ma14092245.

[29] Hong Y, Hu Y, Zhao A. Effects of loading frequency on fatigue behavior of metallic materials – a literature review. Fatigue Fract Eng Mater Struct 2023;46(8):3077–98. https://doi.org/10.1111/ffe.14055.

[30] Pan X, Hong Y. High-cycle and very-high-cycle fatigue of an additively manufactured aluminium alloy under axial cycling at ultrasonic and conventional frequencies. Int J Fatigue 2024;185:108363. https://doi.org/10.1016/j.ijfatigue.2024.108363.

[31] Hong Y, Lei Z, Sun C, Zhao A. Propensities of crack interior initiation and early growth for very-high-cycle fatigue of high strength steels. Int J Fatigue 2014;58:144–51. https://doi.org/10.1016/j.ijfatigue.2013.02.023.

[32] Su H, Liu X, Sun C, Hong Y. Nanograin layer formation at crack initiation region for very-high-cycle fatigue of a Ti-6Al-4V alloy. Fatigue Fract Eng Mater Struct 2017;40(6):979–93. https://doi.org/10.1111/ffe.12562.

[33] Oguma N, Harada H, Sakai T. Mechanism of long life fatigue fracture induced by interior inclusion for bearing steel in rotating bending. J Soc Mater Sci 2003;52:1292–7. https://doi.org/10.2472/jsms.52.1292. in Japanese.

[34] Hong Y, Liu X, Lei Z, Sun C. The formation mechanism of characteristic region at crack initiation for very-high-cycle fatigue of high-strength steels. Int J Fatigue 2016;89:108–18. https://doi.org/10.1016/j.ijfatigue.2015.11.029.

[35] Jiang Q, Sun C, Liu X, Hong Y. Very-high-cycle fatigue behavior of a structural steel with and without induced surface defects. Int J Fatigue 2016;93:352–62. https://doi.org/10.1016/j.ijfatigue.2016.05.032.

[36] Ritz F, Beck T. Influence of mean stress and notches on the very high cycle fatigue behaviour and crack initiation of a low-pressure steam turbine steel. Fatigue Fract Eng Mater Struct 2017;40(11):1762–71. https://doi.org/10.1111/ffe.12666.

[37] Ritz F, Stäcker C, Beck T, Sander M. FGA formation mechanism for X10CrNiMoV12-2-2 and 34CrNiMo6 for constant and variable amplitude tests under the influence of applied mean loads. Fatigue Fract Eng Mater Struct 2018;41(7):1576–87. https://doi.org/10.1111/ffe.12797.

[38] Pan X, Su H, Sun C, Hong Y. The behavior of crack initiation and early growth in high-cycle and very-high-cycle fatigue regimes for a titanium alloy. Int J Fatigue 2018;115:67–78. https://doi.org/10.1016/j.ijfatigue.2018.03.021.

[39] Cong T, Qian G, Zhang G, Wu S, Pan X, Du L, et al. Effects of inclusion size and stress ratio on the very-high-cycle fatigue behavior of pearlitic steel. Int J Fatigue 2021;142:105958. https://doi.org/10.1016/j.ijfatigue.2020.105958.

[40] Du L, Pan X, Qian G, Zheng L, Hong Y. Crack initiation mechanisms under two stress ratios up to very-high-cycle fatigue regime for a selective laser melted Ti-6Al-4V. Int J Fatigue 2021;149:106294. https://doi.org/10.1016/j.ijfatigue.2021.106294.

[41] Du L, Pan X, Hong Y. New insights into microstructure refinement in crack initiation region of very-high-cycle fatigue for SLM Ti-6Al-4V via precession electron diffraction. Materialia 2024;33:102008. https://doi.org/10.1016/j.mtla.2024.102008.

[42] Pan X, Du L, Qian G, Hong Y. Microstructure features induced by fatigue crack initiation up to very-high-cycle regime for an additively manufactured aluminium alloy. J Mater Sci Technol 2024;173:247–60. https://doi.org/10.1016/j.jmst.2023.07.023.

[43] Pan X, Xu S, Nikitin A, Shanyavskiy A, Palin-Luc T, Hong Y. Crack initiation induced nanograins and facets of a titanium alloy with lamellar and equiaxed microstructure in very-high-cycle fatigue. Mater Lett 2024;357:135769. https://doi.org/10.1016/j.matlet.2023.135769.

[44] Zhao J, Jiang Z. Thermomechanical processing of advanced high strength steels. Prog Mater Sci 2018;94:174–242. https://doi.org/10.1016/j.pmatsci.2018.01.006.

[45] Yadegari P, Beier HT, Vormwald M, Kleemann A. Estimation of the fatigue strength of ultra-high strength steels. Procedia Struct Integr 2022;37:500–7. https://doi.org/10.1016/j.prostr.2022.01.115.

[46] Li K, Yang T, Gong N, Wu J, Wu X, Zhang DZ, et al. Additive manufacturing of ultra-high strength steels: a review. J Alloy Compd 2023;965:171390. https://doi.org/10.1016/j.jallcom.2023.171390.

[47] Manjunatha M, Comlekci T, Perez JM, Gorash Y, Mackenzie D. Experimental and numerical investigation on crack propagation in high strength steels and conventional steels. Procedia Struct Integr 2025;68:1223–9. https://doi.org/10.1016/j.prostr.2025.06.191.

[48] M. Huang B. He Y. Li M. Wang High Strength Steels: Microstructure, Properties, and applications 2025 Elsevier Amsterdam, the Netherlands 10.1016/C2022-0-02047-X.

[49] Sakai T, Sato Y, Nagano Y, Takeda M, Oguma N. Effect of stress ratio on long life fatigue behavior of high carbon chromium bearing steel under axial loading. Int J Fatigue 2006;28:1547–54. https://doi.org/10.1016/j.ijfatigue.2005.04.018.

[50] Gao G, Zhang B, Cheng C, Zhao P, Zhang H, Bai B. Very high cycle fatigue behaviors of bainite/martensite multiphase steel treated by quenching-partitioning-tempering process. Int J Fatigue 2016;92:203–10. https://doi.org/10.1016/j.ijfatigue.2016.06.025.

[51] Zhang N, Fu C, Jiang B, Sun L, Liu Y. Failure analysis of fatigue fracture for 60Si2Mn steel fastening clip in the track of high-speed railway. Eng Fail Anal 2022;142:106757. https://doi.org/10.1016/j.engfailanal.2022.106757.

[52] Kanaev AT, Moldakhmetova AE, Kanaev AA, Ramazanova ZM, Sarsembaeva TE. About the optimal range of hardness of wheel and rail steel. Steel Transl 2023;53(7):648–53. https://doi.org/10.3103/S0967091223070069.

[53] Luo Q, Kitchen M, Farmilo N, Li J, Li W, Li Y. Spalling failure mechanism of a railway turnout made from carbide-free bainitic steel. Wear 2025;571:205843. https://doi.org/10.1016/j.wear.2025.205843.

[54] Gao C, Zhang Y, Fan T, Wang J, Song H, Su H. Microstructure and mechanical properties of high-speed train wheels: a study of the rim and web. Crystals 2025;15(8):677. https://doi.org/10.3390/cryst15080677.

[55] Liu L, Ma Y, Liu S, Wang S. The fatigue behaviors of a medium-carbon pearlitic wheel-steel with elongated sulfides in high-cycle and very-high-cycle regimes. Materials 2021;14(15):4318. https://doi.org/10.3390/ma14154318.

[56] Zhou Y, Sun J, Pan X, Qian G, Hong Y. Microstructure evolution and very-high-cycle fatigue crack initiation behavior of a structural steel with two loading intermittence modes. Int J Fatigue 2022;161:106904. https://doi.org/10.1016/j.ijfatigue.2022.106904.

[57] Liu C, Zhang G, Chen C, Liu P, Pan J, Zhang B, et al. Formation mechanism for the white etching microstructure in the subsurface of the failure pearlite wheel steel. Wear 2022;494:204243. https://doi.org/10.1016/j.wear.2022.204243.

[58] Liu Y, Tan Z, Tian Y, Zhu J, Zhang M, Zhang M, et al. Temperature-dependent crack induced by microstructure evolution in 20Mn2SiMoCuV bainite wheel steel. Eng Fail Anal 2022;140:106593. https://doi.org/10.1016/j.engfailanal.2022.106593.

[59] Mazzù A, Zani N, Petrogalli C, Bodini I, Ghidini L, Faccoli M. Experimental investigation on the effect of bainite traces on wear and rolling contact fatigue in ER8 railway wheel steel. Wear 2025;580–1:206264. https://doi.org/10.1016/j.wear.2025.206264.

[60] Sun C, Song Q, Zhou L, Pan X. Characteristic of interior crack initiation and early growth for high cycle and very high cycle fatigue of a martensitic stainless steel. Mater Sci Eng A-Struct 2019;758:112–20. https://doi.org/10.1016/j.msea.2019.04.015.

[61] TB/T 2817-1997. Technical specifications for solid forged and rolled steel wheels for railway vehicles. Beijing: The Ministry of Railways of the People's Republic of China; 1997. (in Chinese).

[62] Astm e8, e8m-24.. Standard test methods for tension testing of metallic materials. West Conshohocken, PA, USA: ASTM International; 2024.

[63] Pilkey WD, Pilkey DF. Peterson's stress Concentration Factors. 3rd ed. Hoboken, NJ, USA: John Wiley & Sons; 2008. https://onlinelibrary.wiley.com/doi/pdf/10.1002/9780470211106.fmatter.

[64] GB/T 13298-2015. Inspection methods of microstructure for metals. Beijing: Standardization Administration of China; 2015. (in Chinese).

[65] Li Z, Zhou S, Yang C, Yong Q. High/very high cycle fatigue behaviors of medium carbon pearlitic wheel steels and the effects of microstructure and non-metallic inclusions. Mater Sci Eng A-Struct 2019;764:138208. https://doi.org/10.1016/j.msea.2019.138208.

[66] Bao D, Cheng G, Zhang J, Wang Z, Li W, Li Y, et al. Characteristics and formation mechanism of oxide-sulfide complex inclusions in high-speed railway wheel steel. Metall Mater Trans B 2024;55(3):1939–50. https://doi.org/10.1007/s11663-024-03078-2.

[67] Pan X, Qian G, Hong Y. Nanograin formation in dimple ridges due to local severe-plastic-deformation during ductile fracture. Scr Mater 2021;194:113631. https://doi.org/10.1016/j.scriptamat.2020.113631.

[68] Haigh BP. Experiments on the fatigue of brasses. J Inst Metals 1917;18:55–86.

[69] Gerber H. Bestimmung der zulässigen spannungen in eisen-konstructionen. Zeitschrift des Bayerischen Architeckten und Ingenieur-Vereins 1874;6:101–10.

[70] Schönbauer BM, Perlega A, Karr UP, Gandy D, Stanzl-Tschegg SE. Pit-to-crack transition under cyclic loading in 12% Cr steam turbine blade steel. Int J Fatigue 2015;76:19–32. https://doi.org/10.1016/j.ijfatigue.2014.10.010.

[71] Schönbauer BM, Ghosh S, Karr U, Pallaspuro S, Kömi J, Frondelius T, et al. Mean-stress sensitivity of an ultrahigh-strength steel under uniaxial and torsional high and very high cycle fatigue loading. Fatigue Fract Eng Mater Struct 2022;45(11):3361–77. https://doi.org/10.1111/ffe.13767.

[72] Pan X, Tao Z, Hong Y. Microstructure-based tensile indicator for assessing high-cycle and very-high-cycle fatigue of titanium alloys with additive and conventional manufacturing. Procedia Struct Integr 2025;68:1038–44. https://doi.org/10.1016/j.prostr.2025.06.167.

[73] Hull D. Fractography: observing, measuring and Interpreting Fracture Surface Topography. Cambridge: Cambridge University Press; 1999. https://assets.cambridge.org/97805216/46840/frontmatter/9780521646840_frontmatter.pdf.

[74] Pan X, Hong Y. High-cycle and very-high-cycle fatigue behaviour of a titanium alloy with equiaxed microstructure under different mean stresses. Fatigue Fract Eng Mater Struct 2019;42(9):1950–64. https://doi.org/10.1111/ffe.13050.

[75] Sistaninia M, Maierhofer J, Spalek A, Gänser H-P, Bucher C, Pippan R, et al. Influence of surface condition, cycling frequency and ferritic zones on the high and very high cycle fatigue properties of a pearlitic steel. Mater Sci Eng A-Struct 2024;900:146483. https://doi.org/10.1016/j.msea.2024.146483.

[76] Tao Z, Chang Y, Pan X, Qian G, Hong Y. Numerical simulation of crack surface contacting behavior with stress-induced martensitic phase transformation in very-high-cycle fatigue regime. Int J Fatigue 2025;198:109019. https://doi.org/10.1016/j.ijfatigue.2025.109019.
[77] Pan X, Tao Z, Long X. Extraordinary specimen-size effect on long-life fatigue of additively manufactured AlSi10Mg. Int J Mech Sci 2025;301:110524. https://doi.org/10.1016/j.ijmecsci.2025.110524.
[78] Wang Y, Wang F, Yu W, Wang Y, Qi Z. Effects of MnS inclusions on mechanical behavior and damage mechanism of free-cutting steel: a molecular dynamics study. J Mol Graph Model 2023;118:108354. https://doi.org/10.1016/j.jmgm.2022.108354.
[79] Qiu G, Du Q, Lu F, Miao D, Yang Y, Li X. Review on regulation of MnS in non-quenched and tempered steel. J Iron Steel Res Int 2024;31:779–89. https://doi.org/10.1007/s42243-023-01146-6.
[80] Tao Z, Wang Z, Pan X, Su T, Long X, Liu B, et al. A new probabilistic control volume scheme to interpret specimen size effect on fatigue life of additively manufactured titanium alloys. Int J Fatigue 2024;183:108262. https://doi.org/10.1016/j.ijfatigue.2024.108262.